

1 **Nonlinear response of extreme precipitation to warming in CESM1**

2

3 **A. G. Pendergrass^{1*}, D. Coleman¹, C. Deser¹, F. Lehner¹, N. Rosenbloom¹, and I.R.**
4 **Simpson¹**

5 ¹National Center for Atmospheric Research, Boulder, CO, USA

6

7 *Corresponding author: Angeline G. Pendergrass (apgrass@ucar.edu)

8

9 **Key Points:**

- 10 • In CESM1, extreme precipitation (the heaviest day each year) is quadratically related to
11 warming in the tropics.
- 12 • Extreme precipitation change is closely related to circulation strength and large-scale
13 precipitation fraction.
- 14 • CESM1 is an end member among its cohort of climate models for this behavior.

15

16

17 **Abstract**

18 The response of extreme precipitation to warming varies widely among climate models,
19 especially in the tropics. In some models, there have been indications that the rate of response
20 increases with warming – that the response is not linear. We investigate the evolution of extreme
21 precipitation, quantified by the maximum accumulated precipitation in a day each year, in
22 CESM1. We find that tropical- and global-average extreme precipitation are related to global-
23 mean surface temperature quadratically. This behavior is associated with an increase in the large-
24 scale fraction of extreme precipitation, and also strengthening circulation on extreme
25 precipitation days. Compared to other CMIP5 models, the nonlinearity in CESM1 is among the
26 largest. One implication is that the difference between CESM1 simulations with full forcing and
27 with fixed aerosols cannot be used to isolate the response of extreme precipitation to aerosols, as
28 the resulting climates are not equally warm.

29

30 **Plain language summary**

31 Extreme precipitation can drive natural disasters like floods and landslides, so understanding and
32 quantifying how it responds to warming is important. Climate models disagree on how much
33 extreme precipitation changes in response to global warming in the tropics. Here we focus on
34 trying to understand this response in just one climate model, CESM1. Some previous studies
35 using this model assumed that the response of extreme precipitation for a given amount of
36 warming is fixed. This is what we would expect if the change in extreme precipitation followed
37 the amount of moisture in the atmosphere. However, we find that the response of extreme
38 precipitation in the tropics to a given amount of warming is not fixed, but instead increases as the
39 temperature warms. Changes in circulation and in the way the model produces precipitation
40 accompany this behavior. Compared to other climate models, this behavior is shared by some but
41 not all models. CESM1 has a larger increase in extreme precipitation change in response to
42 warming than most models, and some lack this behavior entirely. The next generation of models
43 that descend from CESM1 also do not share this behavior.

44

45 **1 Introduction**

46 Climate variability and change can often be approximated as linear: for example, the
47 global average precipitation change from 0 to 1°C of global warming is approximately the same
48 as the change from 1 to 2° in climate model projections. However, for extreme precipitation, that
49 the response to warming in some models might increase as the warming itself increases – a
50 nonlinear response. This type of response occurs in models with a tropical extreme precipitation
51 response that deviates from the response of the rest of the intensity distribution, which has been
52 called an “extreme mode” [Pendergrass and Hartmann, 2014]. The extreme mode is one factor
53 that contributes to the substantial variation in the magnitude of the tropical extreme precipitation
54 response across climate models [O’Gorman, 2012]. This variation in extreme precipitation
55 response also influences non-extreme precipitation; models with larger increases in extreme
56 precipitation have smaller increases or even decreases in non-extreme precipitation [Thackeray
57 *et al.*, 2018].

58 One framework for thinking about extreme precipitation change is that the precipitation
59 rate in an extreme event is proportional to the product of moisture and circulation (measured by
60 vertical velocity through the cloud base, or by convergence of dry air in the boundary layer)
61 [Pendergrass and Gerber, 2016]. In this framework, if moisture were to change at constant
62 relative humidity with no change in circulation, then the extreme precipitation change would
63 follow moisture, deviating only slightly from linearity ($\Delta r_x / r_x$, where r_x is extreme
64 precipitation). In model projections, moisture changes at approximately constant relative
65 humidity, but changes in circulation also contribute to extreme precipitation change (particularly
66 its spatial pattern) [Pfahl *et al.*, 2017].

67 Despite indications that the response of extreme precipitation to warming may not be
68 linear in all climate models, additivity is sometimes assumed. One approach that has been used
69 to isolate the climate response to individual forcing agents is to take the difference between
70 simulations in which many forcings vary over time and simulations in which one forcing is held
71 fixed; this works when the response to each forcing is linear and thus additive. Two recent
72 studies use this approach to try and isolate the extreme precipitation response to anthropogenic
73 aerosol forcing [Lin *et al.*, 2016; Zhao *et al.*, 2018]. However, the linearity of the extreme
74 precipitation response to climate change in these simulations has not been established.

75 Here we investigate the response of extreme precipitation to climate change by focusing
76 on one climate model, CESM1. We will show that the response of extreme precipitation in the
77 tropics is actually nonlinear. Then we will show how this nonlinearity relates to
78 parameterizations of precipitation, as well as changes in circulation and moisture. Next we will
79 compare the response of extreme precipitation in CESM1 with other models from the CMIP5
80 cohort. Finally we will consider the implications for isolating the response of extreme
81 precipitation to GHG and anthropogenic aerosol forcings.

82 **2 Methods**

83 One challenge for studying extreme events is that they are rare; more samples improve
84 our certainty in quantifying these events and how they change. Large ensembles of simulations
85 enable greater sampling, widening the breadth of analyses that can be employed. We use two
86 large ensembles of CESM1 simulations: the 40-member CESM1 Large Ensemble (CESM1-LE)
87 [Kay *et al.*, 2015], and a 20-member ensemble with fixed anthropogenic aerosols (hereafter
88 CESM1-AA). The CESM1-LE is a set of fully-coupled simulations at nominal 1° resolution,
89 forced with historical estimates of natural and anthropogenic radiative forcings from 1920-2005
90 and the Representative Concentration Pathway (RCP) 8.5 scenario [Meinshausen *et al.*, 2011]
91 from 2006 through 2100. RCP8.5 is a high emissions scenario with large increases in GHGs over
92 the 21st century and anthropogenic aerosol forcing which increases until about 2030 and then
93 subsequently decreases to low levels by the end of the century. Members are initialized from
94 year 1920 of a historical simulation that begins in 1850; members are differentiated by adding
95 small perturbations to atmospheric temperature [see Kay *et al.*, 2015]. CESM1-AA is a 20-
96 member set of simulations from 1920-2080, which are identical to the CESM1-LE except that
97 energy-sector anthropogenic aerosols remain fixed at 1920 values. Like CESM1-LE, CESM1-
98 AA members are initialized with small perturbations to atmospheric temperatures in 1920, using
99 the same historical simulation as CESM1-LE. The variables we use here are monthly-averaged
100 reference height air temperature (TREFHT), and daily-averaged precipitation (convective and
101 large-scale, PRECC and PRECL), zonal and meridional wind components at 850 hPa (U850 and

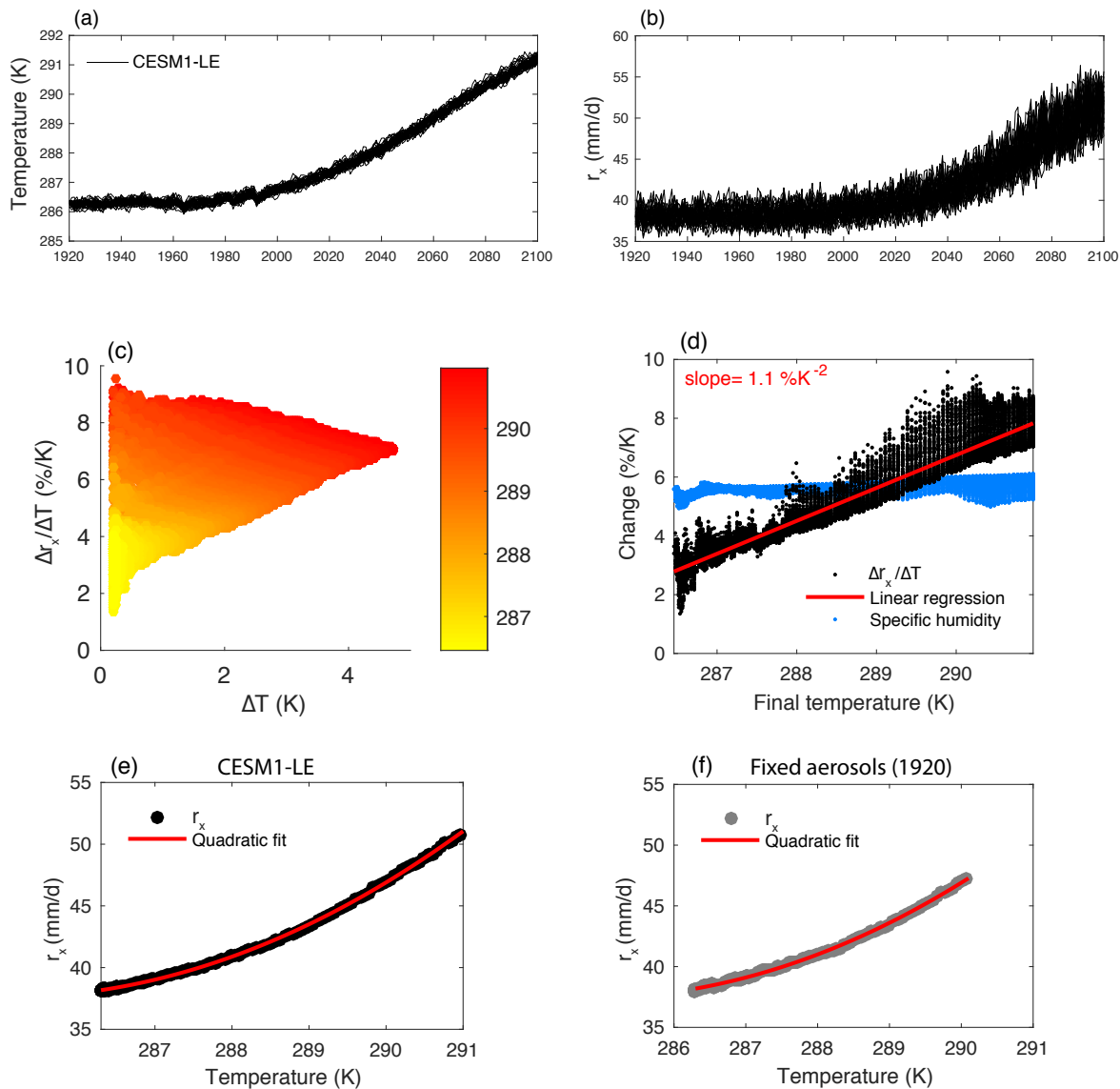
102 V850), specific humidity in the lowest atmospheric layer (QBOT), and 500-hPa vertical velocity
103 (OMEGA500, available for 2 members of the CESM1-LE).

104 We also compare CESM1 against the CMIP5 multi-model ensemble. We use fully
105 coupled historical and RCP8.5 simulations from one ensemble member each of the 33 CMIP5
106 models with daily precipitation and monthly near-surface air temperature.

107 The response of extreme precipitation to global warming depends on how “extreme
108 precipitation” is defined: the more extreme an event is, the larger its response is to warming
109 [*Pendergrass, 2018*]. Here we use the maximum daily accumulation of precipitation in each year
110 (r_x , often called Rx1day, [*Zhang et al., 2011*]). r_x is extreme enough that its behavior does not
111 merely follow mean precipitation [*Pendergrass et al., 2015*]. At observing stations, r_x makes up
112 8.5% of total precipitation [*Pendergrass and Knutti, 2018*]. r_x can be calculated for each year in
113 each ensemble member, which facilitates analysis of changes over time. We calculate r_x at each
114 grid point, and then take area averages – e.g., global, tropical, or extratropical.

115 **3 Response of extreme precipitation to warming in CESM1**

116 In the CESM1-LE simulations, global-mean surface temperature increases little from
117 1920-1980, and subsequently climb upward through 2100 (Fig. 1a). Globally-averaged r_x
118 follows this overall pattern, with little change until 1980 and a subsequent increase (Fig. 1b). The
119 variability of r_x across ensemble members is higher than for temperature, and it also increases
120 over the 21st century.



121

122 **Figure 1.** Nonlinear response of extreme precipitation to warming. Timeseries of (a) global-
 123 mean temperature and (b) maximum daily accumulation of precipitation each year (R_{x1} day or
 124 r_x) in the CESM1-LE 40-member ensemble. (c) $\Delta r_x/\Delta T$ between ensemble mean 10-year epoch
 125 pairs with >0.2 K global-mean temperature increase. Color indicates the global-mean
 126 temperature of the final epoch of the pair, T_{final} . (d) $\Delta r_x/\Delta T$ versus final epoch temperature
 127 (black). The best-fit regression line is shown in red, with the slope indicated at the top left, and
 128 the change in global, annual mean near surface specific humidity in blue. (e) Ensemble-, global-
 129 mean r_x versus temperature for each epoch from panel (d). The red line indicates the best-fit
 130 quadratic polynomial. (f) As in panel (e) for simulations with anthropogenic aerosols fixed at
 131 1920 values (Fig. S1).

132

133 To quantify the rate of change of r_x with warming, one approach is to calculate paired
 134 epoch differences. Some previous studies have, instead, regressed changes in extreme
 135 precipitation against changes in temperature [Pendergrass *et al.*, 2015; Lin *et al.*, 2016], but this
 136 assumes that the changes are linear. For our paired epoch differences, we choose 10-year epochs,
 137 averaging over all 40 ensemble members to reduce noise. We use all possible pairs of epochs,
 138 drawing both the initial and final epochs from the entire course of the simulation. After
 139 calculating global-mean temperature T and r_x for each epoch, we calculate the relative change
 140 normalized by warming ($\Delta r_x / \Delta T$, with units of $\% \text{K}^{-1}$), which is the change in r_x divided by the
 141 average r_x during the base epoch and also ΔT . To avoid redundancy and division by zero, we
 142 exclude epoch pairs whose global-mean temperature change is less than +0.2 K in absolute
 143 value, which has the effect that each pair is a warmer epoch compared to a cooler epoch.

144 Examining $\Delta r_x / \Delta T$ as a function of ΔT , the relationship is not unique (Fig. 1c). For small
 145 warming increments close to the lower threshold (+0.2 K), $\Delta r_x / \Delta T$ ranges from ~ 1 to $\sim 9 \% \text{K}^{-1}$.
 146 Moving toward larger ΔT , the range of $\Delta r_x / \Delta T$ converges to $\sim 7 \% \text{K}^{-1}$ at around 5K warming. In
 147 terms of when in the simulation each epoch pair occurs, the largest ΔT must involve initial
 148 epochs toward the beginning of the simulations (before ~ 1980) with those toward the end. The
 149 epoch pairs with smaller ΔT are from periods closer together in time, or from the beginning of
 150 the simulations. This raises the question: if the rate of extreme precipitation change is not driven
 151 solely by temperature change, what other factors play a role?

152 Motivated by the observation that the variability of r_x increases with warming (Fig. 1b),
 153 we examine $\Delta r_x / \Delta T$ as a function of the temperature of the final (warmer) epoch (T_{final} , Fig. 1c
 154 and d). Unlike ΔT , there is a monotonic relationship between T_{final} and $\Delta r_x / \Delta T$ – larger values
 155 of $\Delta r_x / \Delta T$ occur when the final epoch is warmer. Indeed, linear regression captures much of this
 156 relationship – the slope of the best fit regression line is $1.1 \% \text{K}^{-2}$. There are also features that
 157 linear regression does not capture, including some systematic variation among ensemble
 158 members (e.g. $\sim 287.5 \text{ K}$), which is related to large volcanic eruptions that cool all ensemble
 159 members simultaneously. All large volcanic eruptions in these simulations occur before 2000;
 160 none are present in the future emissions scenario from 2006 onward.

161 If $\Delta r_x / \Delta T$ is linearly related to T_{final} , then by simple calculus we should expect r_x to be
 162 quadratically related to T ,

$$163 \quad \frac{dr_x}{dT} = aT,$$

$$164 \quad \int \frac{dr_x}{dT} dT = \int (aT) dT,$$

$$165 \quad r_x = aT^2 + b.$$

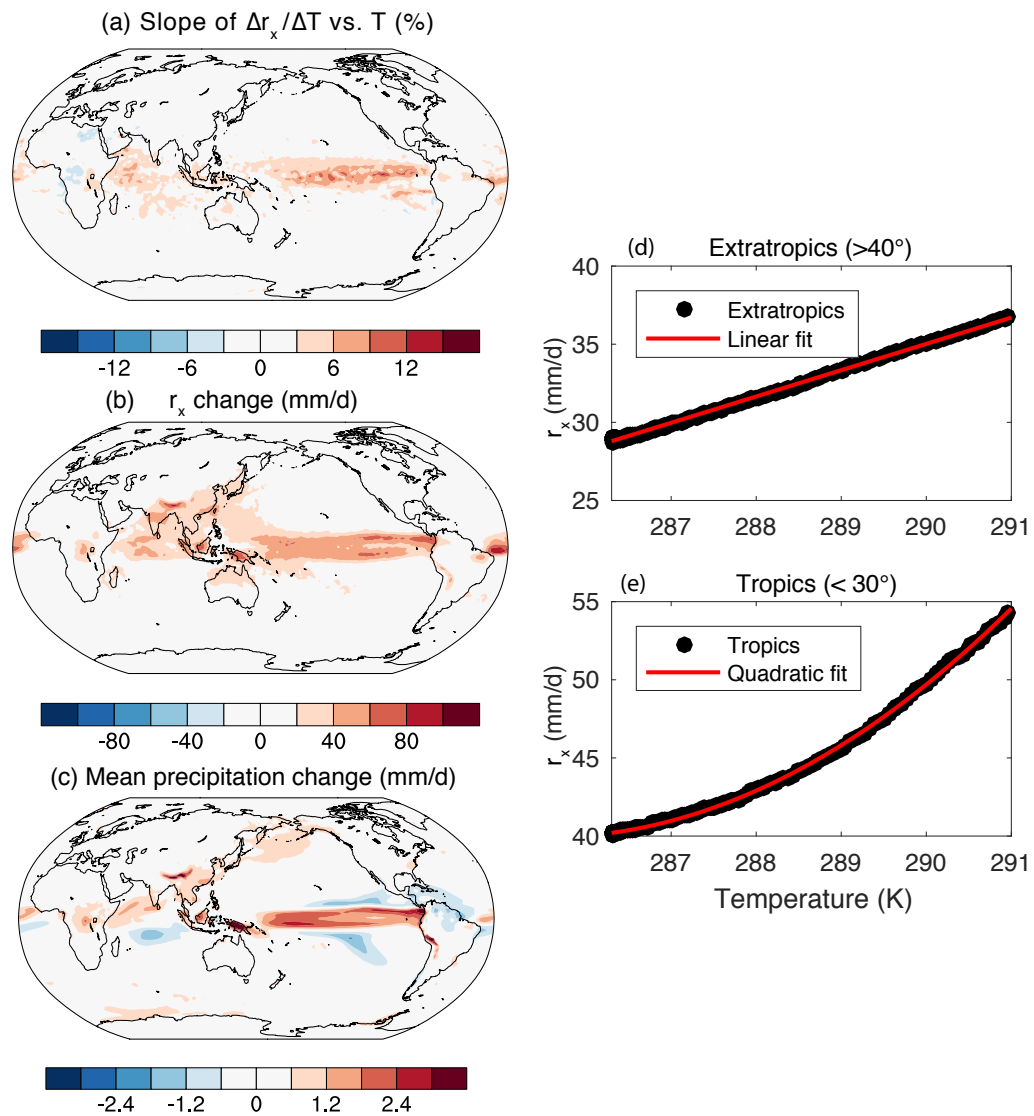
166 Averaging each epoch globally and across all ensemble members, we see that this is indeed the
 167 case (Fig. 1e). Furthermore, averaging across 40 ensemble members removes most noise, so the
 168 quadratic polynomial fit explains over 99.9% of the variance of the relationship between r_x and
 169 T .

170 Recall from section 1 that if circulation during extreme events did not change with
 171 warming, extreme precipitation intensity would change with roughly the rate of moisture
 172 increase. How does the change in extreme precipitation in these simulations compare to changes

173 in moisture? In these simulations, global, annual average specific humidity in the bottom layer of
174 the atmosphere increases by about 5 to 6 % K⁻¹ early in the simulation, rising slightly toward 6 %
175 K⁻¹ by the end of the simulations, a rate slightly lower than Clausius-Clapeyron (CC, Fig. 1d).
176 Specific humidity on the day of heaviest precipitation each year rises at a slightly smaller rate,
177 between 4 and 5.5 % K⁻¹ (not shown). CC is between 6 and 7 %K⁻¹ at temperatures in these
178 simulations, and decreases slightly with temperature. The change in moisture contrasts starkly
179 with $\Delta r_x/\Delta T$, which varies from ~ 3 %K⁻¹ at colder global-mean temperatures to ~ 8 % K⁻¹ at the
180 warmest temperatures.

181 So far we have examined the changes in globally-averaged $\Delta r_x/\Delta T$. But previous work
182 has shown that in models with large increases in extreme precipitation, these occur in the tropics,
183 rather than the extratropics [O’Gorman, 2012; Pendergrass and Hartmann, 2014]. Therefore, we
184 next examine the spatial pattern of the nonlinearity in r_x . To do this, we calculate the slope of the
185 regression line between $\Delta r_x/\Delta T$ at each gridpoint and global T_{final} : a larger slope indicates
186 larger nonlinearity in r_x . For this calculation, we only use time periods from 2000 onwards, to
187 avoid the influence of volcanic eruptions.

188 The slope of $\Delta r_x/\Delta T$ versus T_{final} is positive across the deep tropical oceans and portions
189 of the tropical continents (Fig. 2a). Some regions of Africa have negative slopes. Most of the
190 extratropics have smaller slopes. The spatial pattern has some similarities to the pattern of
191 change in r_x (Fig. 2b), such as the enhanced increases across much of the tropical oceans, but
192 also some differences from it, for example over southeast Asia. The spatial pattern of r_x change
193 also bears some resemblance to mean precipitation change [Fischer *et al.*, 2013; Pendergrass *et*
194 *al.*, 2017, Fig. 2c]: both have increases in the tropical Pacific and Atlantic, the northern Indian
195 Ocean and some tropical land areas. But they differ in that mean precipitation also has regions of
196 decrease.



197

198 **Figure 2.** Geographical patterns of the nonlinear change in extreme precipitation. Maps of (a)
 199 slope of $\Delta r_x / \Delta T$ versus T_{final} , and for 2091-2100 minus 2000-2009, the (b) change in r_x and (c)
 200 mean precipitation change. r_x versus T (d) poleward of 40° latitude with linear fit and (e)
 201 equatorward of 30° with quadratic fit.

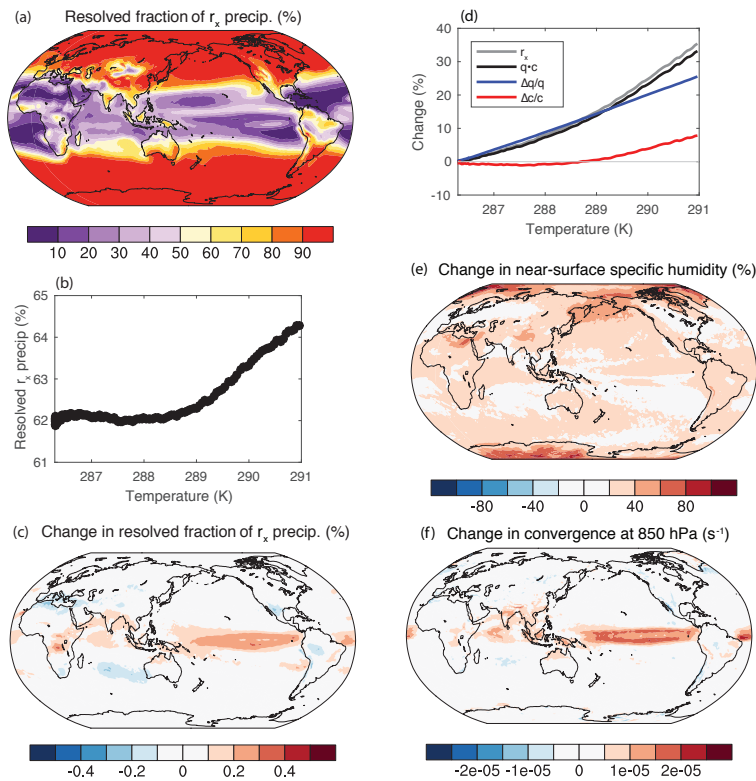
202

203 The spatial pattern motivates us to compare regional averages over the tropics, which we
 204 define as equatorward of 30° latitude, and the extratropics, poleward of 40° . The relationship
 205 between tropical r_x and T is captured well by a quadratic fit, while the relationship between
 206 extratropical r_x and T is nearly linear, consistent with the spatial pattern of nonlinearity.
 207 (Substituting local temperature change or temperature change on each day for global-mean
 208 temperature produces a qualitatively similar result). The nonlinearity, then, arises from the
 209 tropics. It is dominated by the tropical oceans, but remains present when the analysis is restricted
 210 to tropical land (Table S1).

211 What drives the nonlinear relationship between tropical r_x and T ? It has been argued that
 212 aerosol forcing drives a larger extreme precipitation increase than greenhouse gas forcing [*Lin et*
 213 *al.*, 2016]. To test whether the nonlinear extreme precipitation response is driven by aerosol
 214 forcing, we repeat the analysis using the CESM1-AA ensemble, with fixed aerosol forcing. The
 215 nonlinear behavior persists in these simulations (Fig. 1f and S1), which indicates that it is not
 216 driven by these aerosols.

217 Precipitation in climate models, including CESM1 and all other CMIP5 models, is
 218 parameterized – via either convective (unresolved) or large-scale (resolved) parameterizations;
 219 so parameterizations are a potential driver of the nonlinearity. The fraction of r_x falling as
 220 resolved precipitation has a strong dependence on latitude in CESM1 – most extreme
 221 precipitation is resolved in the extratropics, while most is unresolved in the tropics (Fig. 3a). In
 222 the tropics, there are also differences between precipitation over land and ocean; over land, more
 223 precipitation is resolved than over ocean. In response to warming, the fraction of r_x precipitation
 224 that is resolved increases from about 62% to just over 64%, particularly beyond 289 K (Fig. 3b).
 225 The spatial pattern of the increase in resolved r_x fraction (Fig. 3c) bears resemblance to the
 226 change in r_x itself, to the spatial pattern of the nonlinearity (Fig. 2a), and also to the changes in
 227 mean precipitation (Fig. 2c). The increase in resolved fraction of r_x probably plays a role in the
 228 nonlinearity, though some of this role could be merely that regions which newly find themselves
 229 in mean ascent (due to, e.g., the shifting ITCZ) have more resolved extreme precipitation.

230



231

232 **Figure 3.** Parameterization of extreme precipitation; moisture and circulation components of
 233 change. (a) Fraction of r_x arising from resolved (large-scale) precipitation in CESM1, (b) global-

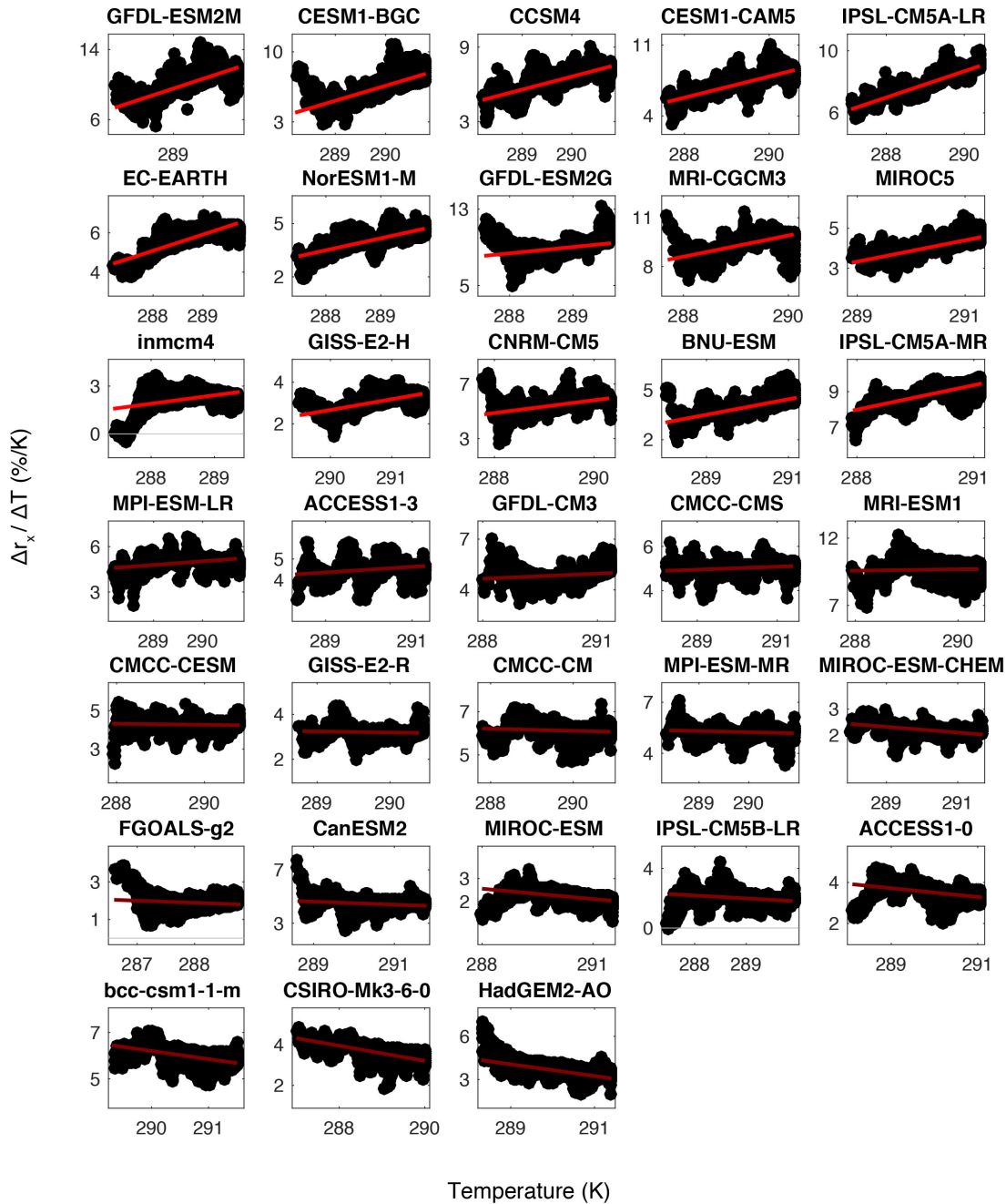
234 mean fraction of resolved r_x at different global-mean temperatures, and (c) spatial pattern of the
235 change in resolved fraction of r_x . (d) Scaling of r_x into circulation, c , and moisture, q ,
236 components: the change in r_x (grey), the change in the product of q and c (approximating r_x ,
237 black), the change in q alone (blue), and the change in c alone (red). Spatial pattern of the
238 change in (e) near-surface specific humidity and (f) 850 hPa convergence on the day of r_x . See
239 supplement for details.

240 The roles of circulation and moisture change can be decomposed using various scaling
241 relationships [e.g., *O’Gorman and Schneider, 2009; Norris et al., 2019*]. To estimate circulation
242 throughout the CESM1-LE simulations (given available model output), we use a single-level
243 scaling between near-surface specific humidity and convergence at 850 hPa (Fig. 3d). This
244 scaling closely captures the changes in r_x , underestimating it slightly (the actual change is 35%
245 compared to scaling of 33% at the end of the simulations). Moisture climbs steadily upward,
246 nearly linearly, consistent with constant-relative humidity warming on r_x days. But convergence
247 strength changes little until about 289 K global-mean temperature and subsequently increases,
248 similar to the resolved fraction of r_x . Convergence at 850 hPa follows a similar trajectory to 500
249 hPa vertical velocity (Fig. S3). The spatial pattern of moisture change (Fig. 3e) resembles that
250 expected based on constant-relative-humidity warming, dominated by polar amplification. But
251 the spatial pattern of change in convergence shares many commonalities with the change in
252 resolved fraction of r_x (Fig. 3f).

253 Together these analyses show that the nonlinear increase in r_x in the tropics is associated
254 with increasing circulation strength and also coincides with an increasing importance of resolved
255 precipitation for r_x . Moisture changes and aerosol forcing, on the other hand, are not sources of
256 nonlinearity.

257 **4 Comparison with other climate models**

258 How does the nonlinear increase in r_x in CESM1 compare to that in other climate
259 models? In the CMIP5 archive, most models have just one or a few simulations available. We
260 therefore adapt the analysis to use one simulation from each model and compute the spatially-
261 averaged r_x and temperature over sliding 30-year windows. We start this analysis in 2000, after
262 the effects of large volcanoes have faded. We calculate global $\Delta r_x / \Delta T$ for each epoch pair
263 against T_{final} (following Fig. 1d). We calculate the regression slope across all epoch pairs, and
264 sort the models from largest to smallest slope (Fig. 4).



265

266 **Figure 4.** Nonlinearity across CMIP5 models. Global $\Delta r_x / \Delta T$ between epoch pairs versus
 267 global-mean T_{final} for each model. Best-fit regression line for each simulation in red; bright red
 268 indicates that the slope is significantly different from zero, dark red indicates it is not. The
 269 significance test assumes that slopes are normally distributed with mean equal to the simulation's
 270 slope and standard deviation equal to the maximum-likelihood-estimated standard deviation of
 271 slopes from CESM1-LE. Simulations are sorted from largest to smallest regression slope.

272

273 The relationships are noisier with just one ensemble member than with 40, despite
 274 averaging over 30- instead of 10-year periods (as in Fig. 1c). If the extreme precipitation change
 275 were linear with respect to warming, $\Delta r_x/\Delta T$ would be constant and so the slope of
 276 $\Delta r_x/\Delta T$ versus T_{final} would be zero. To test whether the regression slopes are nonzero, we
 277 assume slopes follow a normal distribution with standard deviation estimated from the CESM1-
 278 LE regression slopes and mean equal to the slope of each CMIP5 simulation, and test whether
 279 this distribution includes zero at the 95% confidence level. Across CMIP5, 15 of the models
 280 have non-zero slopes, all of which are positive.

281 Among the models with the largest increases in $\Delta r_x/\Delta T$ with warming are those in the
 282 CESM family: CESM1-BGC, CESM1-CAM5, CCSM4, and NorESM1-M. While these models
 283 share heritage, they have similarities and differences. CESM1-BGC and CESM1-CAM5 have
 284 very few differences in configuration from the CESM1-LE; the differences in extreme
 285 precipitation response among these simulations are likely due only to internal variability. On the
 286 other hand, CCSM4 and CESM1-BGC have a different atmospheric physics package (CAM4),
 287 which includes differences in shallow convection, cloud micro- and macro-physics, the aerosol
 288 model, and the radiation scheme. NorESM1-M descends from CCSM4, with an updated aerosol-
 289 cloud-radiation scheme [Bentsen *et al.*, 2012].

290 Other models with large increases in $\Delta r_x/\Delta T$ with warming are GFDL-ESM2M and
 291 IPSL-CM5A-LR. The GFDL-ESM family has the largest overall magnitude of extreme
 292 precipitation change among models, reaching 13-14 % K⁻¹ according to this particular measure.
 293 Previous work shows commensurately larger increases for more infrequent definitions of
 294 extreme precipitation [e.g., Pendergrass and Hartmann, 2014]. This indicates that nonlinearities
 295 could account for some of the large increases of extreme precipitation in response to warming.

296 Repeating the analysis for the extratropical extreme precipitation (poleward of 40°), only
 297 8 of the 33 models have a nonzero change in $\Delta r_x/\Delta T$ with T_{final} , which is positive in all cases;
 298 also, the magnitudes of change vary less among models. For the tropics, 14 models have a
 299 nonzero change in $\Delta r_x/\Delta T$ with T_{final} , also all positive. This is consistent with previous work
 300 showing that model uncertainty in extreme precipitation change arises from the tropics
 301 [O’Gorman, 2012], and that the nonlinearity arises from the tropics as well.

302 Since temperature is related to $\Delta r_x/\Delta T$ in individual models, does it explain the variation
 303 across models? Indeed, T in 2000-2009 is not significantly correlated with $\Delta r_x/\Delta T$ or r_x across
 304 models; perhaps tuning precludes a relationship.

305 The CESM1 model has a variety of descendants in CMIP6, including CESM2 and E3SM.
 306 Applying the analysis to one transient carbon dioxide increase simulation with each of these
 307 models (Fig. S2), both have increases in $\Delta r_x/\Delta T$ in response to warming, but the magnitudes are
 308 smaller than CESM1. In E3SM, the slope of $\Delta r_x/\Delta T$ versus T is 0.2 %K⁻², and in CESM2, it is
 309 0.4 %K⁻² (compared to 0.8-1.5 %K⁻² in for individual CESM1-LE members).

310 **5 Implications for the response of extreme precipitation to GHG and aerosol forcing**

311 A nonlinear response of extreme precipitation to warming makes analysis techniques that
 312 implicitly or explicitly assume additivity problematic; for example, those of Lin *et al.*, [2016]
 313 and Zhao *et al.*, [2018]. They approximated the response to aerosol forcing as the difference
 314 between the CESM1 LE and another 15-member CESM1 ensemble over 2005-2100 in which

315 anthropogenic aerosols were held fixed at 2005 values, invoking an assumption of linearity.
316 Using this approach, they found that $\Delta r_x / \Delta T$ is ~ 2 times larger for aerosol forcing than
317 greenhouse gas forcing.

318 In RCP8.5, aerosol forcing increases from 2006-2030, and then subsequently decreases
319 [Pendergrass *et al.*, 2015]. The decrease of aerosols after 2030 drives additional global warming,
320 beyond that from GHGs. As a result, the fixed-aerosol simulations have less global-mean
321 warming than CESM1-LE (Fig. S5). Given the nonlinear relationship between extreme
322 precipitation and temperature documented here, we should expect the additional warming to
323 drive an increase in extreme precipitation regardless of whether the warming is driven by
324 aerosols or greenhouse gases - it occurs at the same rate in simulations with and without changes
325 in anthropogenic aerosol forcing (Fig. S1).

326 In contrast to extreme precipitation, global-mean precipitation is linear in CESM1
327 simulations (Fig. S6). Lin *et al.*, [2016] also find a large difference in the change in global-mean
328 precipitation in response to GHGs and aerosols, which is expected from the differing effects of
329 these forcings on atmospheric radiative fluxes, consistent with other studies. Some conclusions
330 in Lin *et al.* are further affected by the use of moderate definitions of extreme precipitation, like
331 R95p and R10 – the precipitation falling in these events constitutes a large fraction of total
332 precipitation, and thus should be expected to behave more like mean precipitation than extreme
333 precipitation [Pendergrass and Knutti, 2018].

334 **6 Conclusions**

335 Extreme precipitation – quantified here by the maximum amount of precipitation falling
336 on a single day each year (r_x – changes nonlinearly with respect to global-mean temperature in
337 the tropics in CESM1. The nonlinearity is associated with strengthening circulation (the dynamic
338 component) and with an increase in large-scale (resolved) precipitation with warming. The
339 spatial patterns of the circulation change, the increase in large-scale extreme precipitation
340 fraction, and the nonlinearity have many features in common. Mechanisms that we exclude as
341 drivers of the nonlinear response are the change in moisture (the thermodynamic component) and
342 anthropogenic aerosol forcing.

343 Among the CMIP5 cohort of models, the nonlinearity in CESM1 extreme precipitation is
344 among the largest. CCSM4 also shares this large nonlinearity, but initial analysis with E3SM and
345 CESM2 (which both descend from CESM1) indicate that they do not share this behavior.

346 A previous study mistook the nonlinearity in extreme precipitation in CESM1 for a
347 response to aerosol forcing. Because the relationship between extreme precipitation and surface
348 temperature is nonlinear, the responses of extreme precipitation to different forcing agents are
349 not additive, and so the difference between simulations with many forcing agents and those that
350 exclude one forcing does not accurately reflect the influence of that forcing agent on extreme
351 precipitation.

352 One question arises from these findings: is a nonlinear response of tropical extreme
353 precipitation to warming realistic? Changes in circulation that increase as the climate state
354 becomes warmer may be physical. The short observational record could present a challenge for
355 documenting it on Earth. If the response of extreme precipitation were to grow with warming,
356 then changes that have been observed so far would be smaller than what will occur moving into
357 warmer climates in the future. Future work could seek relationships between observable present-

358 day precipitation and nonlinear responses, for example in terms of their spatial pattern. For the
359 moment, this study shows that we can't always assume that climate is linear – sometimes it's
360 quadratic.

361

362 **Acknowledgments and Data**

363 We thank Mark Webb, Jiawei Bao and Steve Sherwood for helpful discussion. This material is
364 based upon work supported by the National Center for Atmospheric Research, which is a major
365 facility sponsored by the National Science Foundation (NSF) under Cooperative Agreement No.
366 1852977. Portions of this study were supported by the Regional and Global Model Analysis
367 (RGMA) component of the Earth and Environmental System Modeling Program of the U.S.
368 Department of Energy's Office of Biological & Environmental Research (BER) via NSF IA
369 1844590.

370

371 CESM1-LE and CESM1-AA data are available from ESG at
372 <http://www.cesm.ucar.edu/projects/community-projects/LENS/data-sets.html> (CESM1-AA is
373 listed as “xaer”). CMIP5 model output is archived by PCMDI, available from
374 <https://pcmdi.llnl.gov/mips/cmip5>. We also thank Urs Beyerle for CMIP5 data management.
375 E3SM data is available from <https://esgf-node.llnl.gov/search/e3sm/> and CESM2 from
376 <https://esgf-node.llnl.gov/search/cmip6/>. The CESM project is supported primarily by the NSF.
377

378 **References**

- 379 Bentsen, M. et al. (2012), The Norwegian Earth System Model, NorESM1-M – Part 1:
380 Description and basic evaluation, *Geosci. Model Dev. Discuss.*, 5, 2843–2931,
381 doi:10.5194/gmdd-5-2843-2012.
- 382 Fischer, E. M., U. Beyerle, and R. Knutti (2013), Robust spatially aggregated projections of
383 climate extremes, *Nat. Clim. Chang.*, 3(12), 1033–1038, doi:10.1038/nclimate2051.
- 384 Kay, J. E. et al. (2015), The community earth system model (CESM) large ensemble project : A
385 community resource for studying climate change in the presence of internal climate
386 variability, *Bull. Am. Meteorol. Soc.*, 96(8), 1333–1349, doi:10.1175/BAMS-D-13-00255.1.
- 387 Lin, L., Z. Wang, Y. Xu, and Q. Fu (2016), Sensitivity of precipitation extremes to radiative
388 forcing of greenhouse gases and aerosols, *Geophys. Res. Lett.*, 43(18), 9860–9868,
389 doi:10.1002/2016GL070869.
- 390 Lin, L., Y. Xu, Z. Wang, C. Diao, W. Dong, and S.-P. Xie (2018), Changes in Extreme Rainfall
391 Over India and China Attributed to Regional Aerosol-Cloud Interaction During the Late
392 20th Century Rapid Industrialization, *Geophys. Res. Lett.*, 45(15), 7857–7865,
393 doi:10.1029/2018GL078308.
- 394 Meinshausen, M. et al. (2011), The RCP greenhouse gas concentrations and their extensions
395 from 1765 to 2300, *Clim. Change*, 109(1), 213–241, doi:10.1007/s10584-011-0156-z.

- 396 Norris, J., G. Chen, J. D. Neelin, J. Norris, G. Chen, and J. D. Neelin (2019), Thermodynamic
397 versus Dynamic Controls on Extreme Precipitation in a Warming Climate from the
398 Community Earth System Model Large Ensemble, *J. Clim.*, 32(4), 1025–1045,
399 doi:10.1175/JCLI-D-18-0302.1.
- 400 O’Gorman, P. a. (2012), Sensitivity of tropical precipitation extremes to climate change, *Nat.*
401 *Geosci.*, 5(10), 697–700, doi:10.1038/ngeo1568.
- 402 O’Gorman, P. A., and T. Schneider (2009), The physical basis for increases in precipitation
403 extremes in simulations of 21st-century climate change., *Proc. Natl. Acad. Sci. U. S. A.*,
404 106(35), 14773–7, doi:10.1073/pnas.0907610106.
- 405 Pendergrass, A. G. (2018), What precipitation is extreme?, *Science (80-.)*, 360(6393), 1072–
406 1073, doi:10.1126/science.aat1871.
- 407 Pendergrass, A. G., and E. P. Gerber (2016), The rain is askew: Two idealized models relating
408 vertical velocity and precipitation distributions in a warming world, *J. Clim.*, 29(18),
409 doi:10.1175/JCLI-D-16-0097.1.
- 410 Pendergrass, A. G., and D. L. Hartmann (2014), Changes in the distribution of rain frequency
411 and intensity in response to global warming, *J. Clim.*, 27(22), doi:10.1175/JCLI-D-14-
412 00183.1.
- 413 Pendergrass, A. G., and R. Knutti (2018), The Uneven Nature of Daily Precipitation and Its
414 Change, *Geophys. Res. Lett.*, doi:10.1029/2018GL080298.
- 415 Pendergrass, A. G., F. Lehner, B. M. Sanderson, and Y. Xu (2015), Does extreme precipitation
416 intensity depend on the emissions scenario?, *Geophys. Res. Lett.*, 42(20), 8767–8774,
417 doi:10.1002/2015GL065854.
- 418 Pendergrass, A. G., R. Knutti, F. Lehner, C. Deser, and B. M. Sanderson (2017), Precipitation
419 variability increases in a warmer climate, *Sci. Rep.*, 7(1), 17966, doi:10.1038/s41598-017-
420 17966-y.
- 421 Pfahl, S., P. A. O’Gorman, and E. M. Fischer (2017), Understanding the regional pattern of
422 projected future changes in extreme precipitation, *Nat. Clim. Chang.*, 7(6), 423–427,
423 doi:10.1038/nclimate3287.
- 424 Thackeray, C. W., A. M. DeAngelis, A. Hall, D. L. Swain, and X. Qu (2018), On the Connection
425 Between Global Hydrologic Sensitivity and Regional Wet Extremes, *Geophys. Res. Lett.*,
426 doi:10.1029/2018GL079698.
- 427 Zhang, X., L. Alexander, G. C. Hegerl, P. Jones, A. K. Tank, T. C. Peterson, B. Trewin, and F.
428 W. Zwiers (2011), Indices for monitoring changes in extremes based on daily temperature
429 and precipitation data, *Wiley Interdiscip. Rev. Clim. Chang.*, 2(6), 851–870,
430 doi:10.1002/wcc.147.
- 431 Zhao, A. D., D. S. Stevenson, and M. A. Bollasina (2018), The role of anthropogenic aerosols in

432 future precipitation extremes over the Asian Monsoon Region, *Clim. Dyn.*, 1–22,
 433 doi:10.1007/s00382-018-4514-7.

434

435 **Figure captions**

436 **Figure 1.** Nonlinear response of extreme precipitation to warming. Timeseries of (a) global-
 437 mean temperature and (b) maximum daily accumulation of precipitation each year (R_{x1} day or
 438 r_x) in the CESM1-LE 40-member ensemble. (c) $\Delta r_x / \Delta T$ between ensemble mean 10-year epoch
 439 pairs with >0.2 K global-mean temperature increase. Color indicates the global-mean
 440 temperature of the final epoch of the pair, T_{final} . (d) $\Delta r_x / \Delta T$ versus final epoch temperature
 441 (black). The best-fit regression line is shown in red, with the slope indicated at the top left, and
 442 the change in global, annual mean near surface specific humidity in blue. (e) Ensemble-, global-
 443 mean r_x versus temperature for each epoch from panel (d). The red line indicates the best-fit
 444 quadratic polynomial. (f) As in panel (e) for simulations with anthropogenic aerosols fixed at
 445 1920 values (Fig. S1).

446 **Figure 2.** Geographical patterns of the nonlinear change in extreme precipitation. Maps of (a)
 447 slope of $\Delta r_x / \Delta T$ versus T_{final} , and for 2091-2100 minus 2000-2009, the (b) change in r_x and (c)
 448 mean precipitation change. r_x versus T (d) poleward of 40° latitude with linear fit and (e)
 449 equatorward of 30° with quadratic fit.

450 **Figure 3.** Parameterization of extreme precipitation; moisture and circulation components of
 451 change. (a) Fraction of r_x arising from resolved (large-scale) precipitation in CESM1, (b) global-
 452 mean fraction of resolved r_x at different global-mean temperatures, and (c) spatial pattern of the
 453 change in resolved fraction of r_x . (d) Scaling of r_x into circulation, c , and moisture, q ,
 454 components: the change in r_x (grey), the change in the product of q and c (approximating r_x ,
 455 black), the change in q alone (blue), and the change in c alone (red). Spatial pattern of the
 456 change in (e) near-surface specific humidity and (f) 850 hPa convergence on the day of r_x . See
 457 supplement for details.

458 **Figure 4.** Nonlinearity across CMIP5 models. Global $\Delta r_x / \Delta T$ between epoch pairs versus
 459 global-mean T_{final} for each model. Best-fit regression line for each simulation in red; bright red
 460 indicates that the slope is significantly different from zero, dark red indicates it is not. The
 461 significance test assumes that slopes are normally distributed with mean equal to the simulation's
 462 slope and standard deviation equal to the maximum-likelihood-estimated standard deviation of
 463 slopes from CESM1-LE. Simulations are sorted from largest to smallest regression slope.

464

465

Geophysical Research Letters

Supporting Information for

Nonlinear response of extreme precipitation to warming in CESM1

A. G. Pendergrass^{1*}, D. Coleman¹, C. Deser¹, F. Lehner¹, N. Rosenbloom¹, and I.R. Simpson¹

¹National Center for Atmospheric Research, Boulder, CO, USA

*Corresponding author: Angeline G. Pendergrass (apgrass@ucar.edu)

Contents of this file

Text S1
Figures S1 to S4
Table S1

Introduction

This Supporting Information document contains a detailed explanation of the analysis shown in Fig. 3, four additional figures to support arguments made in the text, and one additional table.

Text S1

To calculate the fraction of r_x precipitation arising from resolved (large-scale) precipitation (Fig. 3a-c), for the day of r_x at each grid point for each year, we find the large-scale precipitation (PRECL) and divide it by the total precipitation (r_x , which is also PRECL+PRECC) for that day and grid point. The average over all ensemble members for 2000-2009 is shown in Fig. 3a. The difference from 2000-2009 to 2091-2100 is shown in Fig. 3c. The ensemble, 10-year running, global mean is shown in Fig. 3b.

To calculate the convergence of horizontal winds at 850 hPa on the day of r_x (Fig. 3d,f), we started from daily zonal and meridional winds at 850 hPa (U850 and V850), which were archived for every ensemble member in the CESM1-LE. First, we calculate the horizontal divergence of these fields each day during each simulation, and then multiply by minus one to obtain the convergence. Then, we find the day of r_x for each year at each grid point, and extract the horizontal convergence. The maps of change in horizontal convergence of the day of r_x (Fig. 3f) and near-surface specific humidity (QBOT) on the day of r_x (Fig. 3e) each show the difference of the ensemble average from 2000-2009 to 2091-2100; the map of change in convergence on the day of r_x shows the absolute difference (with units of s^{-1}), while the map of change in near-surface specific humidity on the day of r_x shows the difference relative to the 2000-2009 values (in %).

To decompose r_x into circulation (or convergence) and moisture components (Fig. 3d), we start with the global, ensemble, 10-year running mean of horizontal convergence on the day of r_x (c), near-surface specific humidity on the day of r_x (q), and r_x . The scaling is the product of the global, ensemble, 10-year average c and q ($s = c * q$); the black line in Fig. 3d shows $\Delta s/s$ (in %) relative to 1921-1930 values (all changes in Fig. 3d are calculated relative to this same base period). The gray line in Fig. 3d shows $\Delta r_x/r_x$ for comparison. The blue line shows the change in moisture, $\Delta q/q$, and the red line shows the change in horizontal convergence, $\Delta c/c$.

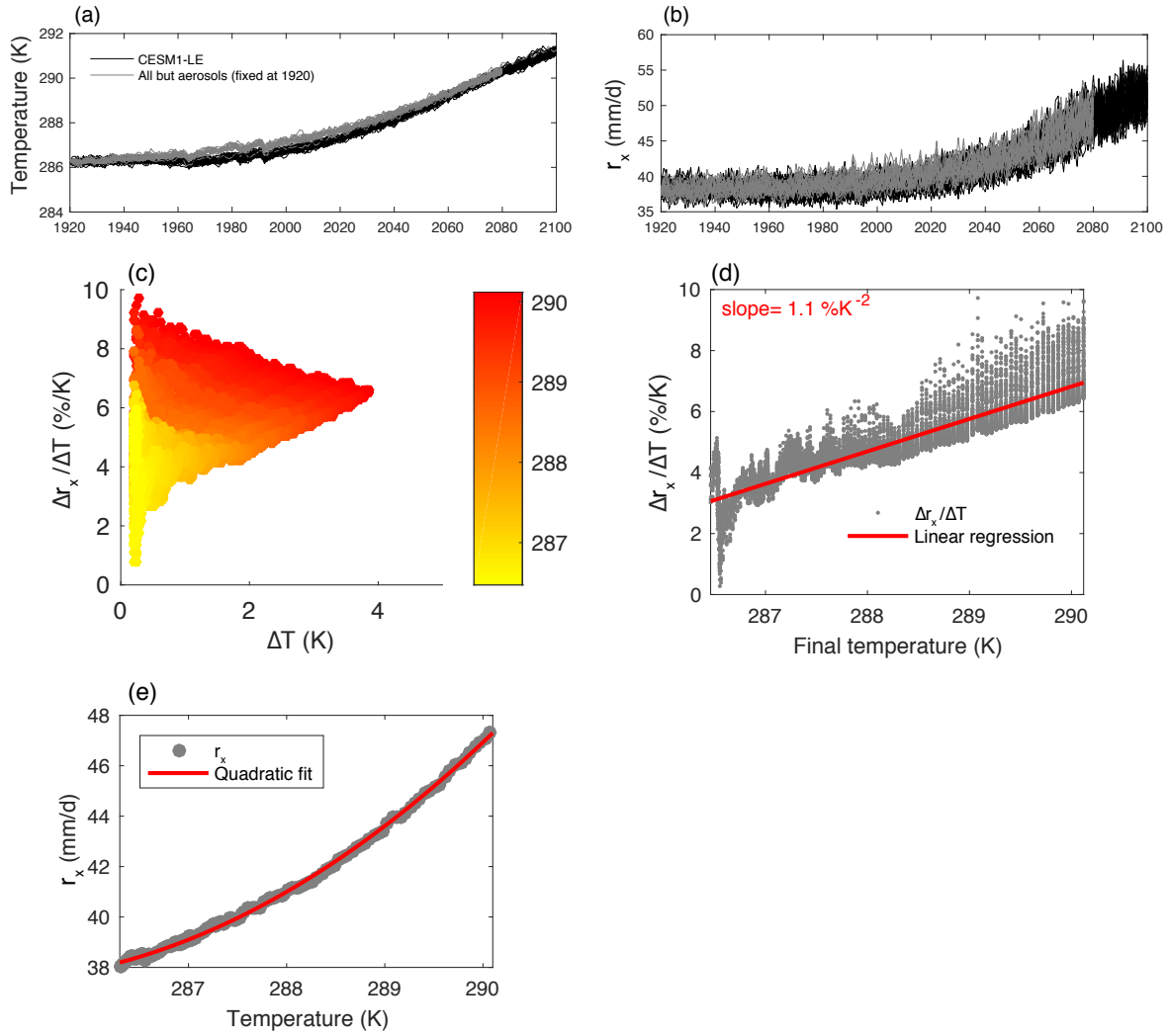


Figure S1. Nonlinear response of extreme precipitation to warming in simulation with fixed anthropogenic aerosol forcing. Following Fig. 1 with a 20-member CESM1 ensemble with anthropogenic aerosol forcing fixed at 1920 values.

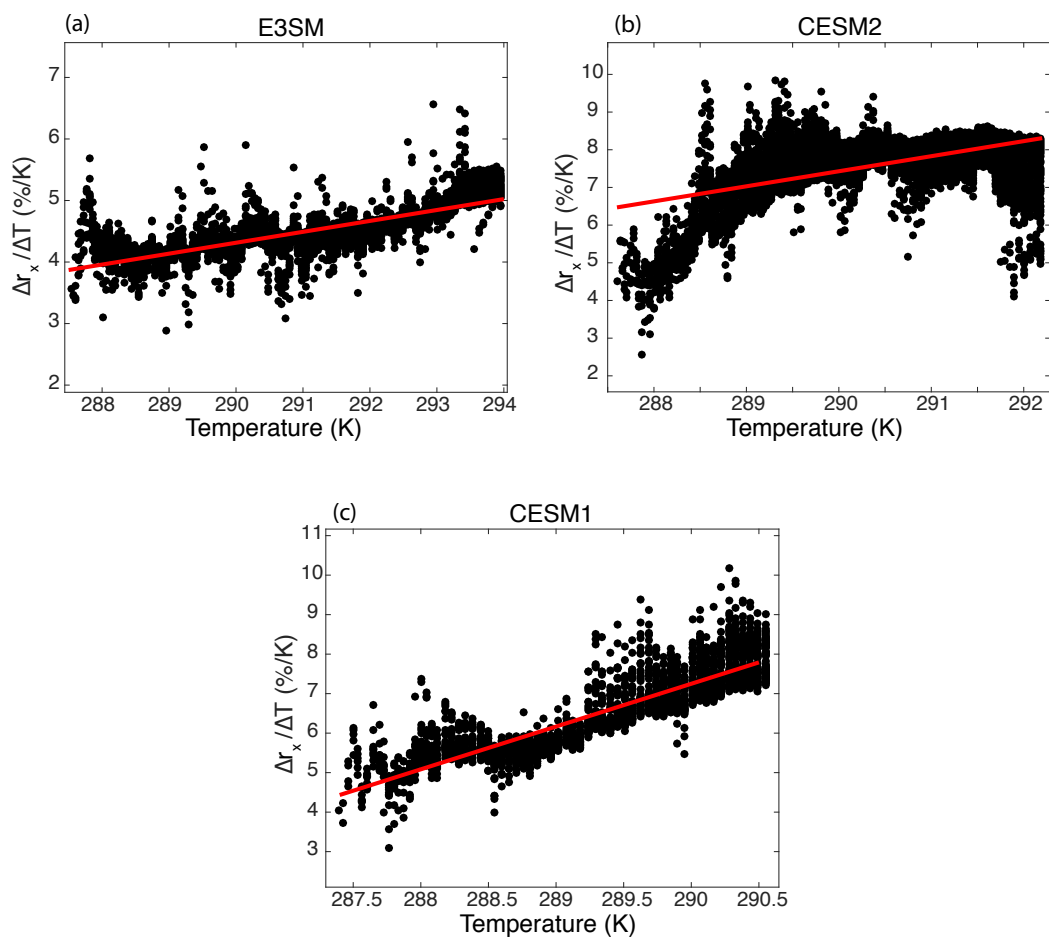


Figure S2. Change in extreme precipitation for (a) E3SM and (b) CESM2, two descendent models of CESM1. (b) The same analysis on one member of the CESM1-LE shown for comparison. Following Fig. 4, for 1pctCO2 CMIP6 DECK experiments.

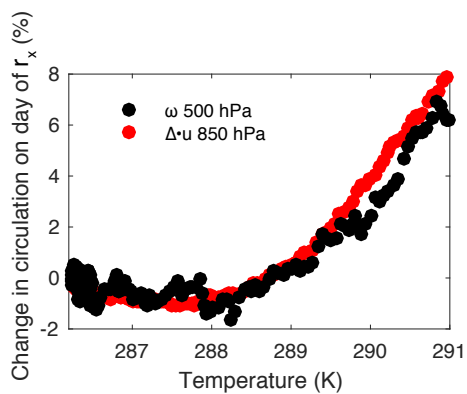


Figure S3. Two ways of quantifying the dynamic component: vertical pressure velocity at 500 hPa and horizontal convergence at 850 hPa.

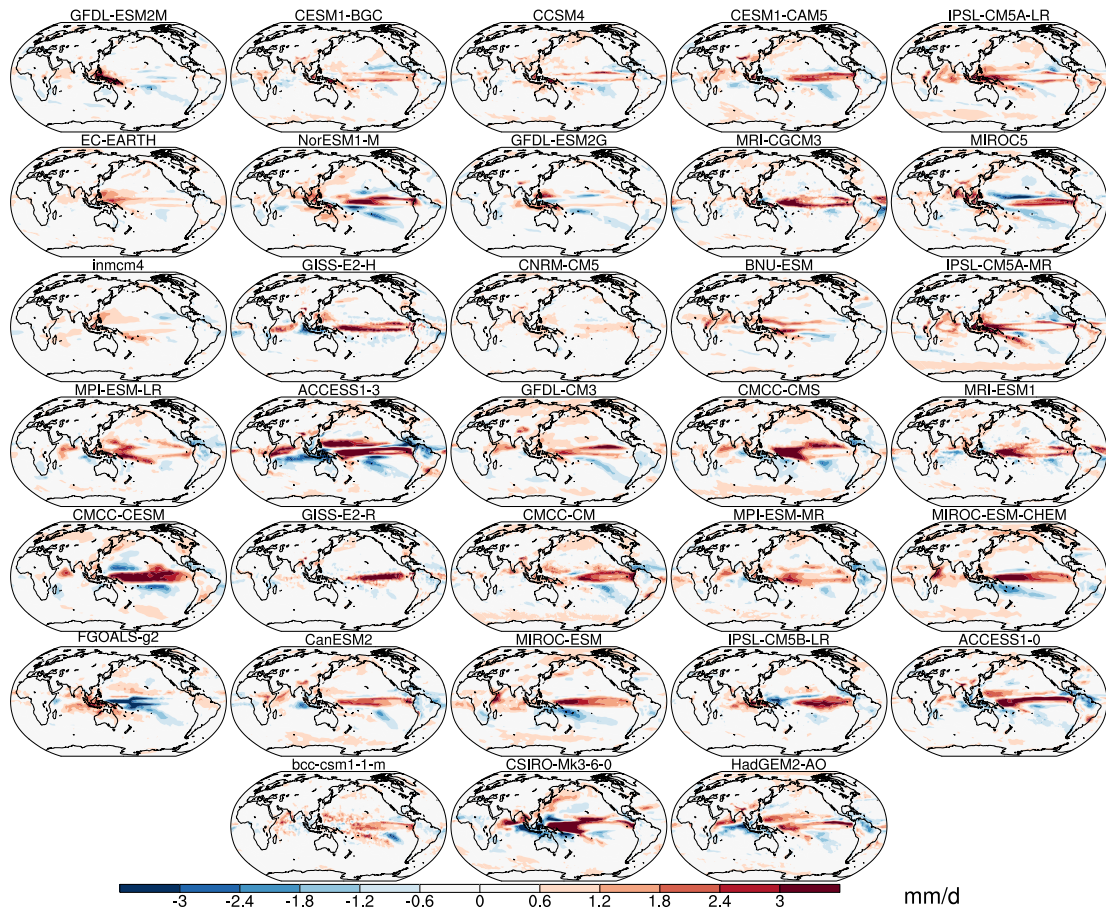


Figure S4. Geographical pattern of mean precipitation change for CMIP5 models. Each map shows the 2091-2100 minus 2000-2009 pattern of precipitation change (compare with Fig. 2c). Model order corresponds to Fig. 4.

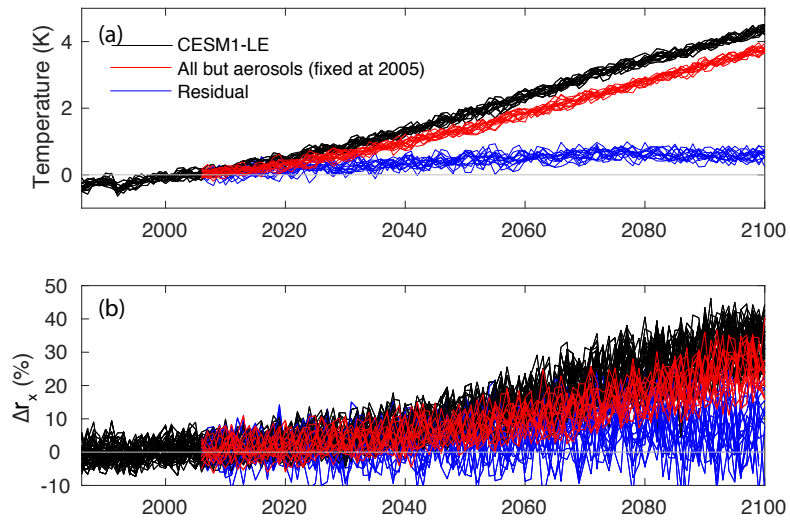


Figure S5. Timeseries of (a) global mean near surface air temperature anomaly and (b) change in maximum day of precipitation averaged globally each year (relative to 1986-2005 mean) for CESM1-LE simulations (black), 15 member ensemble with anthropogenic aerosols fixed at 2005 values (red), and the difference between them (blue).

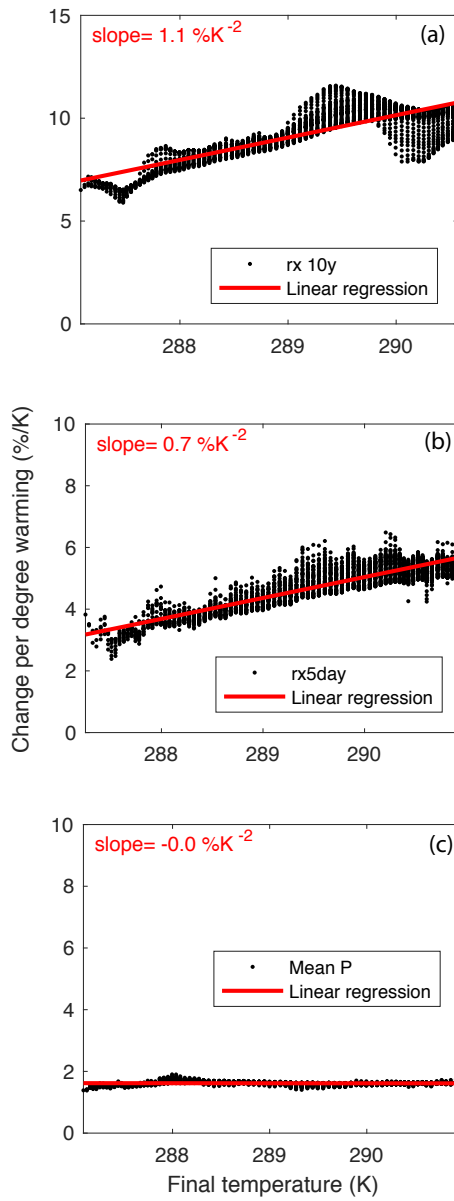


Figure S6. Variation of nonlinearity for different definitions of extreme precipitation. Following Fig. 1d (global mean) for (a) the maximum daily precipitation accumulation every 10 years, (b) the maximum consecutive 5-day accumulation each year (rx5day annual), and (c) mean precipitation.

	Global	Extra-tropics	Tropics	Land	Extratropical land	Tropical land
$\Delta r_x / \Delta T$ slope (%K ⁻²)	1.2	0.2	1.9	0.4	0.0	0.7

Table S1. The slope of $\Delta r_x / \Delta T$ in CESM1-LE over 2000-2100 (analogous to that reported in Fig. 1d), but averaged over different combinations of tropics (<30°), extratropics (>40°), land and combined land and ocean.